01 Jan 2022

The Role of Microstructure on High-Temperature Oxidation Behavior of Hafnium Carbide

Jonathan A. Scott

Xiaoqing He

David W. Lipke
Missouri University of Science and Technology, lipked@mst.edu

Recommended Citation

J. A. Scott et al., "The Role of Microstructure on High-Temperature Oxidation Behavior of Hafnium Carbide," *Journal of the American Ceramic Society*, Wiley, Jan 2022.
The definitive version is available at https://doi.org/10.1111/jace.18941

Received: 19 July 2022 | Revised: 17 October 2022 | Accepted: 22 November 2022

DOI: 10.1111/jace.18941

Journal of the American Ceramic Society

RESEARCH ARTICLE

The role of microstructure on high-temperature oxidation behavior of hafnium carbide

Jonathan A. Scott[1] | **Xiaoqing He**[2] | **David W. Lipke**[1]

[1]Department of Materials Science and Engineering, Missouri University of Science and Technology, Rolla, Missouri, USA

[2]Electron Microscopy Core and Department of Mechanical & Aerospace Engineering, University of Missouri, Columbia, Missouri, USA

Correspondence
David W. Lipke, Department of Materials Science and Engineering, Missouri University of Science and Technology, Rolla, MO 65409, USA.
Email: Lipke@mst.edu

David W. Lipke is a Member, American Ceramic Society.

Funding information
U. S. Office of Naval Research, Grant/Award Number: N00014-17-1-2931

Abstract

Microstructure development of the products formed upon oxidation of hafnium carbide (HfC_x, $x = 0.65$, 0.81, or 0.94) at 1300°C and 0.8 mbar oxygen pressure was investigated using Raman spectroscopy, X-ray diffraction, electron microscopy, and electron energy-loss spectroscopy. For all specimens a multilayered oxide scale was observed featuring an outermost porous hafnia layer and an interlayer adjacent to the parent carbide containing hafnia interspersed with carbon. The outermost hafnia features coarse pores presumably formed during initial stages of oxidation to allow rapidly evolving gaseous products to escape from the oxidation front. As the oxidation scale thickens, diffusional resistance results in slower oxidation rates and smaller quantities of gaseous products that are removed via networks of increasingly fine pores until the local oxygen partial pressure is sufficiently low to selectively oxidize the parent carbide. Electron microscopy studies suggest that the oxidation sequence at this stage begins with the transformation of parent carbide to an amorphous material having empirical formula HfO_2C_x that subsequently phase separates into hafnia and carbon domains. Hafnia polymorphs in the phase-separated region vary from cubic to monoclinic as grains coarsen from ca. 2–20 nm, respectively. Immediately adjacent to the phase-separated region is carbon-free mesoporous hafnia whose pore morphology is inherited from that of prior carbon domains. The average pore size and pore volume fraction observed in mesoporous hafnia are consistent with predictions from kinetic models that ascribe gaseous diffusion through a pore network as the rate determining step in oxidation behavior of hafnium carbide. These observations imply that high-temperature oxidation behavior of hafnium carbide under the employed test conditions is linked to microstructure development via phase separation and coarsening behaviors of an initially formed amorphous HfO_2C_x product.

KEYWORDS
carbides, electron microscopy, oxidation, ultra-high temperature ceramics

1 | INTRODUCTION

Ultrahigh-temperature ceramics (UHTCs) are a class of materials principally comprising Group IV–V transition metal borides, carbides, and nitrides that, on account of their ultrahigh melting points (>3000°C), are candidate materials for service in extreme environment applications such as leading edges of hypersonic vehicles.[1–4] Hafnium carbide (HfC_x) is among the most refractory UHTCs, possessing a melting temperature $T_M = 3950 \pm 40$°C for $x = 0.94 \pm 0.01$.[5] The primary oxidation product of HfC_x, hafnium oxide (HfO_2), melts at ca. 2800°C,[6] making HfC_x particularly attractive for use in high temperature oxidizing environments.

Pure, dense HfC_x is known to form multilayered oxidation scales in test environments ranging from static furnaces to arc-jets corresponding to a variety of test temperatures and oxygen partial pressures.[7–10] Reportedly, the parent carbide is initially saturated with oxygen to form HfC_xO_y where y is <0.10 at 1650°C,[9] followed by the formation of a pore-free interlayer whose composition is variously given by different authors as $HfO_{2-x}C_y$ "where x is small compared to 2 and y is probably closer to 0 than 1,"[10] or as formed via the proposed reaction $HfC_{1-x}O_x + \left(1 - \frac{x}{2}\right) O_2 \rightleftarrows HfO_2 + (1-x)\,C$, with up to 25.5 at.% hafnium, 49.8 at.% oxygen, and 24.5 at.% in the product layer immediately adjacent to the parent carbide.[11] Several diffusion-based models have been put forward to rationalize experimental observations based on a transformation sequence starting from the oxygen-saturated parent carbide, to a carbon-containing interlayer, and finally to hafnia upon continued oxidation. These models make different assumptions concerning rate-limiting transport mechanisms responsible for the kinetics of scale formation. In the model put forward by Bargeron et al.,[11] a moving boundary formalism is used to interpret the parabolic kinetics of oxide layer growth. Bargeron et al. concluded that inward lattice diffusion of oxygen is likely rate-limiting based on the presence of microstructural features generally consistent with this mechanism as seen in high-temperature oxidation of metals, namely, planar interfaces normal to the growth direction and apparent chemical homogeneity of the interlayer at the analytical length scale discernable by electron microprobe. However, the model provides reasonable parabolic rate constants and effective diffusion coefficients, it does not account for the effects of oxidation scale microstructure. Alternatively, Holcomb et al.[12] interpreted the high-temperature oxidation behavior of HfC_x using a counterflow model which assumes that the rate-limiting mechanism is capillary diffusion of gaseous species through a network of pores. The capillary diffusion model predicts parabolic oxidation constants for HfC_x across a range of temperatures and oxygen partial pressures that are consistent with observations using a two-parameter fit for pore volume fraction (ca. 0.02) and pore radius (ca. 0.01 μm).

Despite the success of the model of Holcomb et al. to explain macroscopic oxidation behavior of HfC_x, the processes responsible for pore formation and oxide scale evolution in the vicinity of the carbide–oxide interface remain unclear. This work reports on oxidation studies of HfC_x ($x = 0.65$, 0.81, or 0.94) at 1300°C and 0.8 mbar oxygen pressure aimed at disambiguation of the mechanisms of microstructure development in oxidation scale formation in this technologically important UHTC material.

2 | EXPERIMENTAL PROCEDURES

Hafnium carbide powder (>99.9%, −325 mesh; H.C. Starck, Newton, MA) with a measured composition of $HfC_{0.94}$ was mixed with hafnium hydride powder (min. 95%, max. $d_{50} = 6.0$ μm, Albemarle, Langelsheim, Germany) via ball milling using ethanol and yttria-stabilized zirconia milling media to produce powder mixtures targeting three different compositions of HfC_x. These powder mixtures were subsequently dried using a rotary evaporator and passed through a 50-mesh sieve. Each powder mixture was then loaded into a 1-in. diameter circular graphite die lined with 0.005-in. thick graphite foil (NeoGraf Solutions, Lakewood, OH). The powder compacts were subsequently densified to >95% relative density, either by hot pressing at 2200°C and 32 MPa for 2 h or by spark-plasma sintering at 2200°C and 50 MPa for 5 min. Any flashing or graphite foil left from sintering was removed by surface grinding (FSG-618; Chevalier; Santa Fe Springs, CA). Density was measured via the Archimedes method following a modified version of ASTM B962-17[13] where specimens were boiled for 2 h, rather than 24 h, in distilled water. The carbon content of the pressed specimens was measured using a carbon analyzer (CS600; LECO Corporation; St. Joseph, MI) on powders of crushed bulk specimens that had been passed through a 200-mesh sieve. Pressed discs were mounted in an acrylic resin (VariDur 20-3756; Buehler, Lake Bluff, IL), polished to a 0.25 μm finish, and analyzed using scanning electron microscopy (SEM) to determine average grain size. For $HfC_{0.65}$ and $HfC_{0.81}$, a thermal etching treatment at 1800°C for 30 min was necessary to reveal grain boundaries. At least 300 grains observed from multiple random fields of view were analyzed with image analysis software (ImageJ; National Institutes of Health; Bethesda, MD) via intercept method using 20 lines per sample on three fields of view for each specimen.

Hot pressed specimens were cut into ca. 4 × 4 × 4 mm cubes and subsequently oxidized in an atmosphere-controlled tube furnace under flowing Ar at a rate of 100 ml/min until the furnace temperature reached 1300°C, at which point the furnace atmosphere was switched to a flowing Ar/O_2 gas blend with an O_2 partial pressure of 0.8 mbar for an oxidation test duration of 4 h. Oxygen concentrations were monitored using an oxygen analyzer with ppm sensitivity (AMETEK Thermox CG1000 Oxygen Analyzer; AMETEK; Pittsburgh, PA). Oxidized specimens were mounted, sectioned, and polished to a 0.25 μm finish, and their oxide scales were investigated using optical microscopy, SEM, Raman spectroscopy (LabRAM Aramis; HORIBA Jobin Yvon; Kyoto, Japan), and X-ray diffraction (XRD) (X'Pert MRD; Malvern PANalytical Ltd.; Malvern, UK). For one $HfC_{0.94}$ specimen, tape was used to mechanically separate the oxide scale from the underlying carbide material and was subsequently analyzed following the same experimental procedure. Raman spectra were collected from 500 to 3000 cm^{-1} using an HeNe laser (λ = 632.8 nm). Prior to analysis, spectrometer calibration was performed using a silicon standard. XRD scans were performed in a standard Bragg–Brentano geometry using Ni-filtered Cu-K_α radiation as well as in an azimuthal geometry to generate pole figures used to characterize crystallographic texturing in parent $HfC_{0.94}$ specimens and as-formed oxide scales.

A focused ion beam (FIB) (Scios DualBeam FIB SEM; FEI; Hillsboro, OR) was used to lift out specimens perpendicular to the interface between the HfC_x and oxide scale interlayer, which were subsequently analyzed using transmission electron microscopy (TEM) (Tecnai TF30 Twin; FEI; Hillsboro, OR) and scanning transmission electron microscopy (STEM). Electron energy-loss spectroscopy (EELS) was used to determine the elemental chemistry of selected regions in the vicinity of the interlayer. Due to sample availability, detailed electron microscopy analyses of the interface region immediately adjacent to oxidizing parent carbide grains were primarily conducted on samples of $HfC_{0.94}$.

Berkovich-tip nanoindentation measurements were carried out on polished cross sections of oxidized $HfC_{0.94}$ specimens for the determination of both hardness and Young's modulus values for the oxide scale, interlayer, and the parent carbide material using an Agilent G200 nanoindenter (Keysight Technologies, Santa Rosa, CA). Indentations were created on each specimen using a 200 mN max. load, applied in 10 cycles per indentation, and holding for 10 s at the maximum load. Twenty indentations were made for the parent $HfC_{0.94}$ material and the outer HfO_2 layer, whereas nine indentations were made for the interlayer.

TABLE 1 Relative densities and average grain sizes of SPS-synthesized HfC_x specimens

Composition	Relative density (%)	Average grain size (μm)
$HfC_{0.65\pm0.01}$	97.4 ± 0.1	57 ± 2
$HfC_{0.81\pm0.02}$	95.8 ± 0.1	19 ± 1
$HfC_{0.94\pm0.01}$	94.7 ± 0.1	2 ± 1

3 | RESULTS AND DISCUSSION

3.1 | Origins and role of the HfC_x interlayer

Table 1 lists the measured compositions, relative densities, and average grain sizes of synthesized HfC_x specimens. Significant grain growth in the $HfC_{0.65}$ and $HfC_{0.81}$ specimens was observed with maximum measured grain sizes of 180.7 and 58.0 μm, respectively. XRD analyses of the sintered HfC_x specimens indicated the presence of only HfC with no detectable second phases. Comparison of observed versus expected relative peak intensities showed no evidence of crystallographic texturing in parent carbide materials.

Optical micrographs of oxidized HfC_x specimens are shown in Figure 1A–C. All specimens exhibited similar oxide scale morphologies featuring a multilayered "Maltese cross" shape where the oxide scale is cracked and split at edges. This shape, thought to form due to tensile thermal-elastic mismatch stresses in the oxide scale concentrated at specimen corners and edges,[14] became less pronounced for specimens with lower carbon content. The thickness of the dark innermost layer of the oxide scale (i.e., the "interlayer") increases with carbon content for identical oxidation conditions: 5 ± 1 μm for $HfC_{0.65}$, 11 ± 2 μm for $HfC_{0.81}$, and 20 ± 1 μm for $HfC_{0.94}$. Adjacent to the interlayer/oxide scale (IL/OS) boundary, a region of fine porosity (i.e., having pore radii as small as 12 nm) is observed. Pore size and total apparent porosity increase with distance away from the IL/OS boundary consistent with previous reports.[10,15–17] Based on the analysis of FIB liftouts, pore size was found to increase linearly up to ca. 3 μm away from the IL/OS boundary (Figure 2).

On all specimens, the interlayer is found to contain carbon and hafnia as determined by Raman spectroscopy, the results of which are shown in Figure 3. *D* and *G* peak ratios produced $I(D)/I(G)$ values of 1.24 ($HfC_{0.94}$), 1.77 ($HfC_{0.81}$), and 1.69 ($HfC_{0.65}$), indicating disordering and defectiveness of the graphitic carbon in each specimen.[18] The *D* peak is also downshifted from ~1350 to ~1332 cm^{-1} in all specimens. This is due to the dispersive nature of the *D* peak with the wavelength of the laser used (λ_{HeNe} = 632.8 nm), which causes the excitation energy

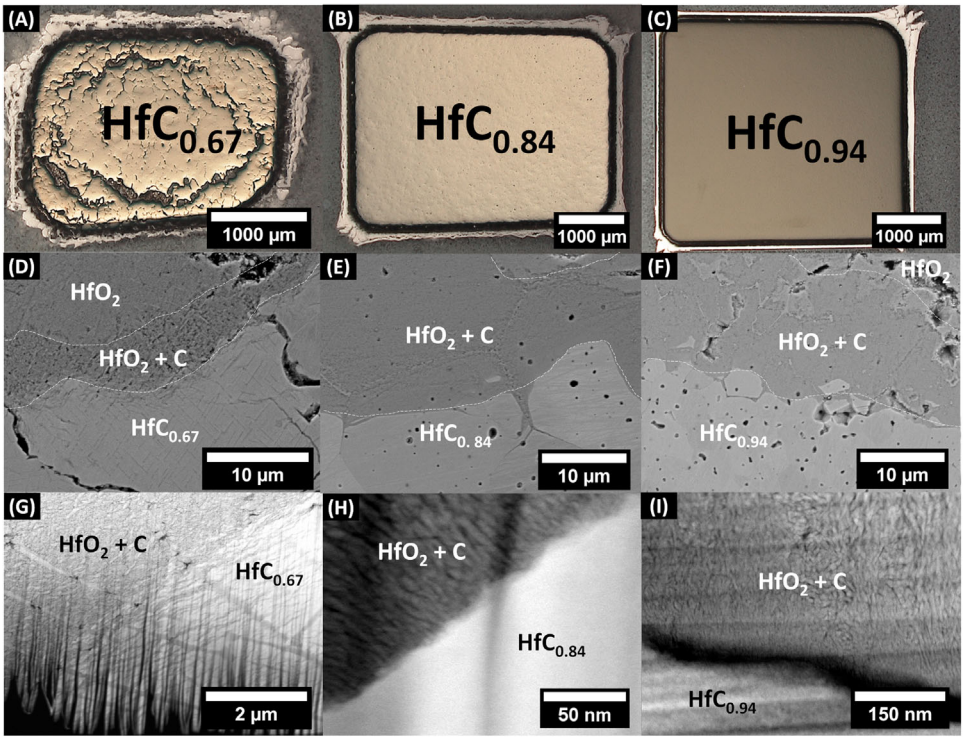

FIGURE 1 Composite image showing the observed morphology of the oxide scale/interlayer material as a function of carbon content. (A–C) Optical micrographs showing macroscopic scale morphology comprising carbide cores surrounded by a multilayered oxidation scale. Polishing damage is evident for the coarse grained $HfC_{0.65}$ specimen. (D–F) Scanning electron microscopy (SEM) images showing the innermost interface for each specimen as a function of carbon content. (G–I) Scanning transmission electron microscopy (STEM)-HAADF images showcasing the differences in oxide scale morphology of the interlayer as a function of carbon content. At "low" carbon contents, microstructure development is markedly different than at "intermediate" and "high" carbon contents.

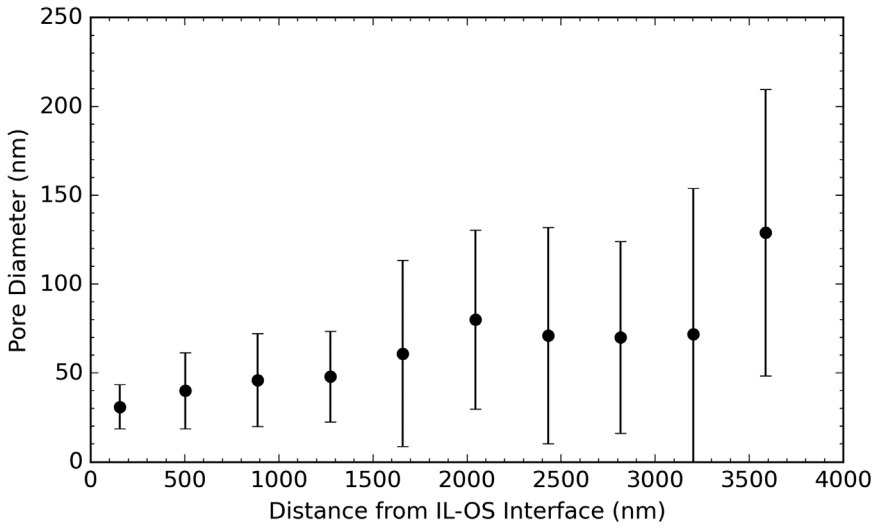

FIGURE 2 Plot of pore size (diameter) as a function of distance from the interlayer-oxide scale interface on $HfC_{0.94}$

required for a Raman scattering event to be reduced and correspondingly reduces the wavenumber at which the *D* peak occurs.[18,19] The shape of the 2D peak located at ~2661 cm^{-1} also indicates that the graphitic carbon is multiple layers thick, as it is beginning to approach the shape of the 2D peak for bulk graphite.[19] Raman spectra of the outer oxide scale indicate only the presence of hafnia, as no *D* or *G* peaks associated with free carbon were identified.

Figure 4 shows XRD patterns of the top surfaces of the oxidized HfC_x specimens. The topmost m-HfO_2 phase formed upon all three compositions exhibits strong

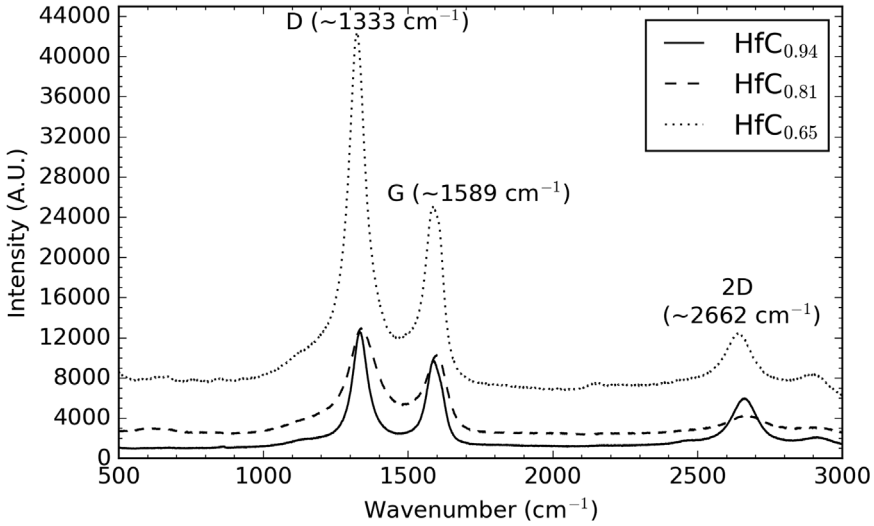

FIGURE 3 Raman spectra collected from the innermost oxide scale of the oxidized HfC_x specimens. Peaks attributed to graphitic carbon dominate the spectrum, but some trace peaks of hafnia can be observed at lower wavenumbers.

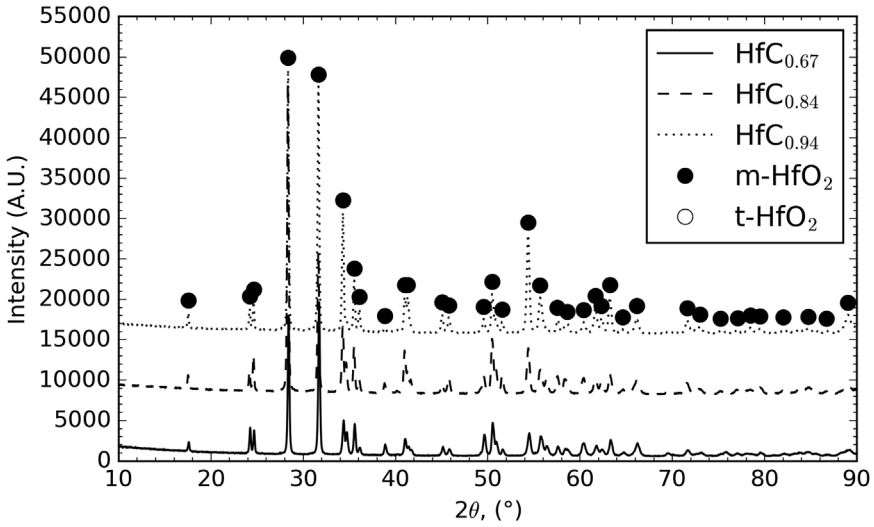

FIGURE 4 X-ray diffraction (XRD) patterns (Cu-K_α $\lambda = 0.1541$ nm) of the top surface of the oxide scale on oxidized $HfC_{0.65}$, $HfC_{0.81}$, and $HfC_{0.94}$

intensity changes in the (202) and ($\bar{2}$02) reflections as compared to its expected pattern (PDF 01-074-1506), indicative of crystallographic texturing (see, e.g., Figure S1 for XRD pole figure analyses of the topmost m-HfO_2 phase formed upon $HfC_{0.94}$). The X-ray pattern for $HfC_{0.94}$ contains diffraction peaks for monoclinic hafnia (m-HfO_2) with trace amounts of tetragonal hafnia (t-HfO_2). XRD scans performed on exposed interlayer product from the oxidation of $HfC_{0.94}$ indicate the presence of m-HfO_2 as well as t-HfO_2 and trace graphite. The 100% intensity peak for t-HfO_2 was not directly observed in these measurements, likely due to spectral resolution issues preventing deconvolution of the t-HfO_2 (101) and $CaCO_3$ (104) peaks (29.651° vs. 29.406°, respectively), with the latter, a constituent of the duct tape backing used to mechanically separate the oxide scale to expose the interlayer for analysis.[20] The amount of t-HfO_2 present could not be quantitatively determined via Rietveld refinement because of texturing effects within the pattern as well as the low intensity of the reflections associated with this phase.

TEM observations of the oxide scale that forms immediately upon grains of $HfC_{0.94}$ show a grain-by-grain orientation dependence indicative of preferential HfO_2 growth directions, for example, if an observed HfC grain is oriented with [111] normal to the surface of the sample, then the (111) plane of HfO_2 appears to grow preferentially. HfO_2 grains whose preferred growth directions are closest to the normal of the oxidation front appear to "win out" and are believed to lead to the observed texturing in the oxide scale even in the absence of any crystallographic texturing in the underlying parent carbide.[21]

TEM micrographs collected near the parent $HfC_{0.94}$-interlayer (PC/IL) boundary provide insights into the initial stages of oxidation. Based on HRTEM shown Figure 5E and Fourier fast transforms (FFT) of the HRTEM shown in Figure 6A, there is an amorphous band of oxide material surrounding the parent carbide grain. Electron diffraction patterns in this region show no long-range order/crystalline diffraction spots. This amorphous band

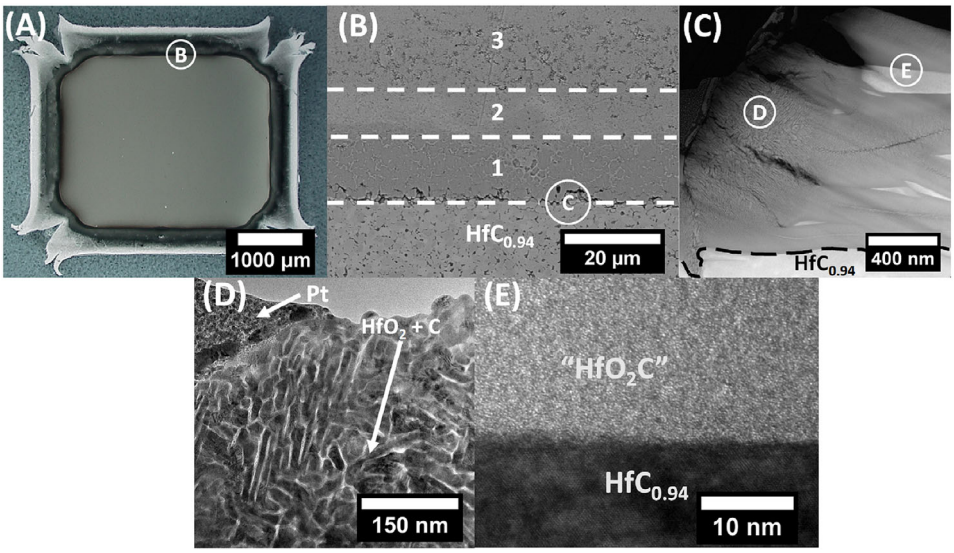

FIGURE 5 Oxidation products of $HfC_{0.94}$ ($T = 1300°C$, $pO_2 = 0.08$ kPa, $t = 4$ h) from macro- to nanoscale. Letters in circles indicate the representative region of the corresponding panel. (A) Optical micrograph of an oxidized HfC specimen showing the "Maltese cross" shape. (B) Scanning electron microscopy (SEM) image of the oxide scale showing three distinct layers. (C) Scanning transmission electron microscopy (STEM)-HAADF image of the interface between HfC and zone 1, which possesses an initially amorphous material around the vicinity of the HfC that proceeds to phase separate. (D) Bright-field transmission electron microscopy (TEM) image showing the fine phase separation of the oxide scale into crystalline HfO_2 (dark) and graphite (bright). (E) Close-up BF TEM image of the amorphous material near grains of HfC

of material persists 20 ± 2 nm away from the parent carbide grain before it begins to phase separate, leading to the nanoscale structures shown in Figures 1G–I and 5D. As viewed under HRTEM, the phase-separated region appears to comprise hafnia and disordered graphitic carbon with ~3.4 Å *d*-spacing. The defected nature of the carbon domain corroborates increased D peak intensities seen in Raman spectra as shown in Figure 3. Gasparrini et al. and Shimada et al. also observed interlayer structures in specimens of zirconium carbide oxidized comprising amorphous carbon and nanocrystalline zirconia precipitates[14,22]; however, the amorphous layer observed herein contains no precipitates.

EELS and EDS chemical analysis of the amorphous region formed upon $HfC_{0.94}$ indicated compositions of $HfO_{2.1}C_{1.0}$ and $HfO_{1.9}C_{0.9}$, respectively. This overall elemental composition likely indicates that the phase forms via selective oxidation where hafnium is oxidized without any loss of carbon. Selective oxidation is a process wherein a compound or solution is exposed to an oxygen chemical potential sufficient to induce oxidation of thermodynamically less noble constituents, whereas more noble constituents remain stable. This phenomenon may be illustrated using a predominance diagram as shown in Figure 7. If the partial pressure of oxygen at the PC/IL interface at 1300°C and 1 bar total pressure is between 1×10^{-21} and 2×10^{-17} bar, then selective oxidation is predicted to occur and result in two equilibrium phases (i.e., graphite and m-HfO_2).

Microstructure development of the oxide scale is consistent with the sequence shown schematically in Figure 8. During the initial stages of oxidation prior to the formation of a protective outer oxide scale, the local oxygen pressure at the parent carbide boundary is sufficiently high to oxidize both Hf and carbon. The total pore volume and average pore size at a given location within the oxide scale is thought to reflect the necessary interconnected pathways to allow gaseous oxidation products to escape from the reaction front through the pore network via Poiseuille flow in proportion to their rate of generation.[12,17] Thus, in the absence of microstructure evolution by diffusion or plastic flow, the observed distribution of porosity through the thickness of the oxide scale acts as a record of the specimen oxidation rate history (i.e., regions with higher amounts of coarse porosity correspond to initially fast oxidation rates, with subsequent decreases in the amount and size of porosity chronicling progression toward a passive oxidation regime). As the oxide scale becomes increasingly protective, diffusive transport becomes rate limiting and overall oxidation kinetics slow, resulting in decreased rates of gaseous product generation. Consequently, scale porosity needed to accommodate escaping gases decreases, which is reflected in observed reductions in apparent pore size approaching the interlayer as shown in Figure 2. Increasing diffusive resistance serves to reduce the oxygen partial pressure at the parent carbide boundary until selective oxidation of Hf becomes thermodynamically favorable and an interlayer forms. Then,

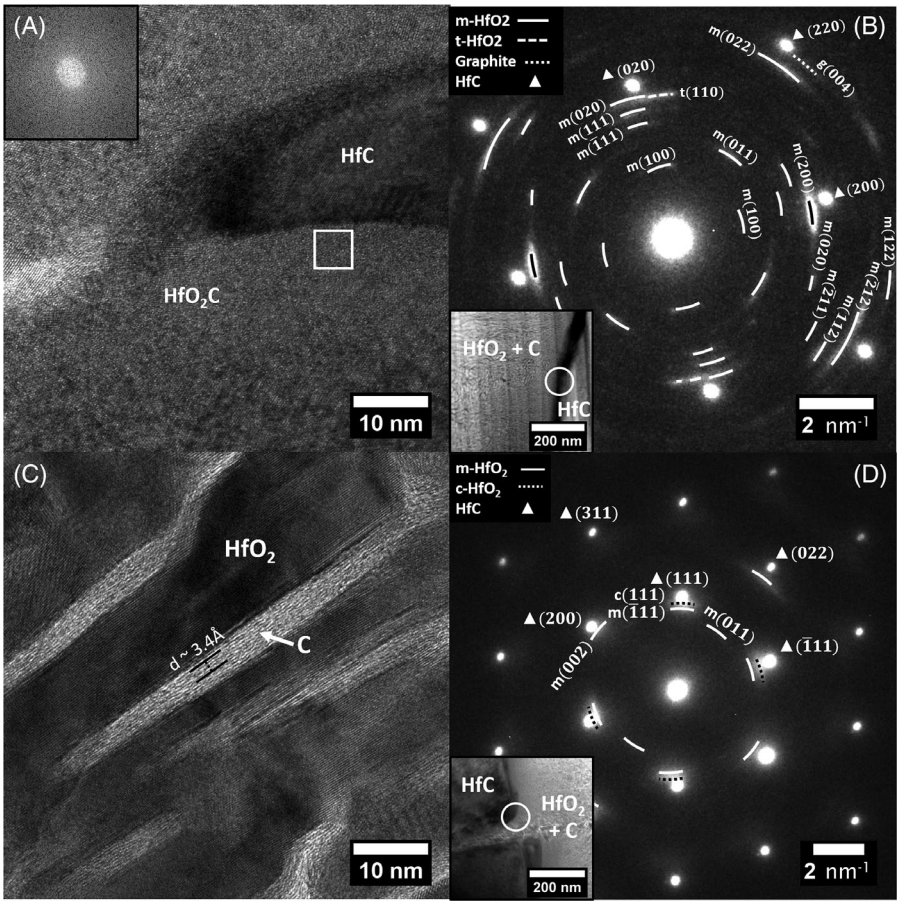

FIGURE 6 (A) Brightfield transmission electron microscopy (TEM) image with an inset Fourier fast transforms (FFT) showing the amorphous nature of the initial oxide scale. (B) Selected area electron diffraction (SAED) pattern of a TEM lift-out near the phase-separated region along the [001] zone axis of $HfC_{0.94}$ containing crystallites of t-HfO_2 and graphite. (C) Brightfield HRTEM image of phase-separated HfO_2 (dark) and C (bright) after crystallization and coarsening. (C) (002) lattice fringes are visibly buckled and distorted. (D) SAED pattern of a TEM lift-out near the amorphous region along the [1$\bar{1}$0] zone axis of HfC. Textured m- and c-HfO_2 that were polycrystalline in nature were detected, as was C.

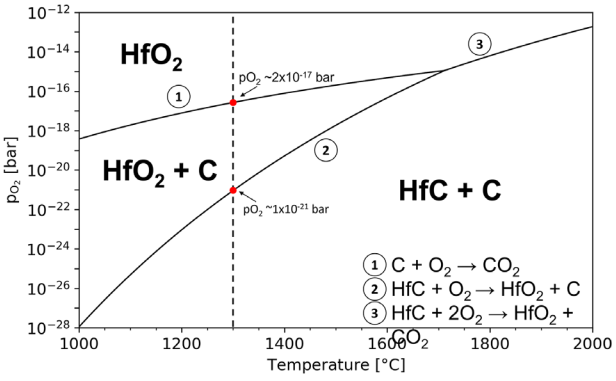

FIGURE 7 Predominance diagram showing the regions of phase stability during the oxidation of stoichiometric HfC at 1 bar total pressure. Carbon refers to graphite as reference state.

the oxidation transformation sequence can be described in three steps: formation of an amorphous HfO_2C_x upon the oxygen-saturated parent carbide; phase separation of the amorphous material into carbon and hafnia domains; and, finally, removal of carbon resulting in a network of fine pores at the IL/OS boundary.

The characteristic size of pores near the IL/OS boundary is commensurate with the final observed degree of coarseness of the carbon domains in the adjoining phase-separated interlayer. In addition, the area fraction of pores measured by image thresholding corresponds to the approximate volume percentage of carbon in the starting material, further supporting that the amount and size of pores in this region are inherited from the phase-separated carbon network. Threshold image analysis on three 1 μm × 1 μm regions in the outer oxide scale yielded an average pore fraction of 22% ± 4%, which is close to the volume fraction of carbon calculated from the molar volumes and stoichiometric coefficients of HfO_2 and C (~20%). Threshold image analysis of the interlayer carbon area fraction resulted in values of 19%. The observed porosity near the IL/OS boundary is consistent with values

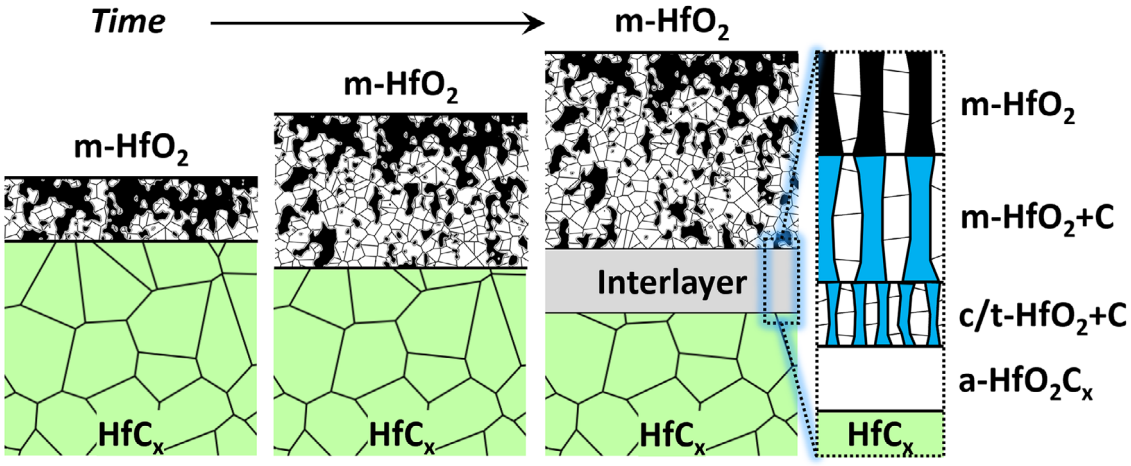

FIGURE 8 Schematic illustration of high-temperature oxidation of HfC. First, HfO_2 oxide scales with coarse porosity are formed. Subsequently, the size and total volume of porosity is reduced in proportion to the rate of oxidation at the PC/IL interface. If a sufficiently protective oxide scale is formed, then the local oxygen pressure at the PC/IL interface eventually reaches a threshold for selective oxidation of hafnium with carbon formation. The transformation sequence then proceeds from an initial amorphous HfO_2C_x product that phase separates into c/t-HfO_2 + C followed by polymorphic transformations to lower symmetry HfO_2 as crystallites coarsen. The IL/OS interface denotes oxidation of phase-separated carbon domains to yield a fine scale pore network that apparently controls the rate of gaseous diffusion and thereby determines high-temperature oxidation kinetics of HfC.

calculated by Holcomb et al. using their countercurrent diffusion model, supporting gaseous diffusion through a fine pore network as the rate limiting kinetic mechanism for HfC_x oxidation.[12] Consequently, high-temperature oxidation behavior of HfC_x is linked to the phase separation behavior of the amorphous oxidation product and its subsequent coarsening kinetics.

3.2 | Additional observations concerning HfC_x oxidation scale

TEM/STEM observations indicate that the phase-separated domains present in the interlayer evolve as a function of crystallite size according to the following sequence: amorphous HfO_2C_x > phase separated c-HfO_2 + C > t-HfO_2 + C > m-HfO_2 + C. The size-dependent stability of HfO_2 polymorphs has been explained by Sharma et al. based on a surface energy relaxation model that predicts a sequence starting from amorphous HfO_2 at a crystallite size less than 3.75 nm, to c-HfO_2 at crystallite sizes ranging 3.75–21 nm, then t-HfO_2 between 21 and 38 nm and finally m-HfO_2 at the largest crystallite sizes.[23] Selected area electron diffraction patterns (Figure 9B) and FFTs of HRTEM patterns of the oxidized material (see Figure S2) show that c-HfO_2 is the first crystalline polymorph that nucleates upon phase separation and that the magnitude of the crystallite size transitions appears consistent with literature. Traces of c-HfO_2 could be detected on the HfC_x side of the PC/IL boundary. When amorphous HfO_2C_x is not present and the HfO_2 crystallites have coarsened appreciably, only spots corresponding to t-HfO_2 and m-HfO_2 are present in the SADPs.[24–26] At the OS/IL boundary, the sizes of HfO_2 crystallites were seen to vary across the tested compositions. For $HfC_{0.94}$, the crystallites were 17–20 nm wide and ~140 nm long, whereas for $HfC_{0.65}$, the crystallites were ~50 nm wide while remaining similar in length (~154 nm) to $HfC_{0.94}$. These elongated crystallites are likely responsible for the texturing effects observed in XRD; however, based on available data, it remains unclear whether parent carbide composition, grain size, or other factors are responsible for the observed differences in HfO_2 crystallite sizes.

The origins of texturing can also be observed from the amorphous region as shown in Figure 6C. As the interlayer material is initially developing, HfO_2 and C begin to phase separate and develop a columnar structure that grows outward, eventually impinging on neighboring phase-separated domains, leading to the structures shown in Figures 1G–I and 5C. The same type of growth behavior was observed in $HfC_{0.81}$; however, significant differences were noted with regards to $HfC_{0.65}$, as shown in Figure 1G. In $HfC_{0.65}$, the phase-separated HfO_2 and C structures appear to grow with the elongated axis parallel to the PC/IL boundary, resulting in discernibly larger crystallites of HfO_2.

Nanoindentation measurements performed on the oxidation products of $HfC_{0.94}$ supports the conclusion that the interlayer is composed of a discrete, phase-separated

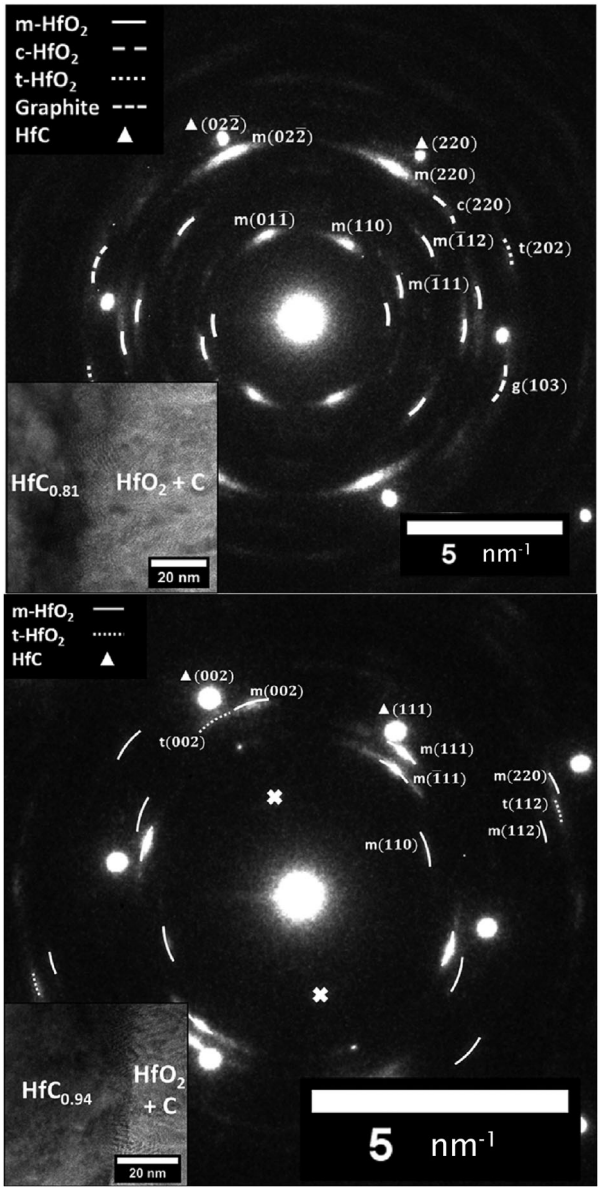

FIGURE 9 Selected area electron diffraction (SAED) patterns of (A) $HfC_{0.81}$ along $[1\bar{1}\bar{1}]$ zone axis and (B) $HfC_{0.94}$ along $[\bar{1}10]$ zone axis. Epitaxial growth with a slight misorientation is present in both cases.

mixture of hafnia and carbon. Results of nanoindentation analyses are summarized in Table 2. For the HfO_2 phase, measured Young's moduli are in close agreement with values reported for nanoindentation performed on HfO_2 thin films; however, measured hardness values are lower than reported for HfO_2 thin films.[27] In several indentation load–displacement curves, crack pop-in behavior was observed, likely due to the presence of microcracks and porosity in the outer oxide layer.

Nanoindentation measurements of parent carbide Young's modulus and hardness indicate values that are lower than those reported for microindentation

TABLE 2 Berkovich-tip nanoindentation results for the Young's modulus and hardness of the different sample zones of $HfC_{0.94}$

Young's modulus (GPa)	Hardness (GPa)	Reference
Parent carbide		
343 ± 19	19 ± 2	This work
N/A	9.5	[10]
350	15	[28]
Interlayer		
150 ± 20	3.3 ± 0.9	This work
N/A	9.7	[10]
Outer oxide scale		
85 ± 18	3.3 ± 1.1	This work
N/A	2.9	[10]
82	4.9	[27]

and nanoindentation of bulk specimens, but that are consistent with values reported for nanoindentation of HfC coatings.[28,29] The hardness values measured for the interlayer material were found to closely match that of the outer oxide layer. This observation is in disagreement with the assessment by Bargeron et al. that the interlayer hardness is comparable to that of the startaqing carbide.[10] However, these differences might be ascribed to different measurement techniques, as a Berkovich indenter was used in the nanoindentation measurements in the present study, whereas Bargeron et al. used a Knoop indenter.[10] Alternatively, given the higher oxidation temperatures used by Bargeron et al. in their study, it is possible that an interlayer material with different properties was produced as compared to the phase-separated interlayer material reported in this work. Additional study of the interlayer formed upon oxidation as a function of temperature may disambiguate this discrepancy.

4 | CONCLUSIONS

The primary conclusion from this work is that the high-temperature oxidation behavior of HfC_x is linked to the phase separation behavior of the first amorphous oxidation product HfO_2C_x and its subsequent coarsening kinetics. This conclusion is supported by observation of microstructure evolution of the products formed upon oxidation of dense (>95% theoretical density) HfC_x (x = 0.65, 0.81, or 0.94) at 1300°C and 0.8 mbar oxygen pressure as characterized by Raman spectroscopy, XRD, electron microscopy, electron energy-loss spectroscopy, and nanoindentation. At early stages of oxidation, generation of large volumes of gaseous products leads to the formation of highly

porous oxide scale. As the scale thickens, diffusive resistance lowers the oxygen partial pressure at the parent carbide boundary until selective oxidation may occur. Subsequently, the interlayer comprising the selective oxidation products of hafnia and carbon may be formed. At this stage, the HfC_x oxidation sequence comprises oxygen saturation of the parent carbide followed by transformation to amorphous HfO_2C_x, phase separation into turbostratic carbon and hafnia polymorphs varying from cubic to tetragonal/monoclinic as crystallite domains coarsen from ~2–20 nm, and finally carbon removal via oxidation from the phase-separated interlayer. The porosity in the oxide scale immediately adjacent to the interlayer appears to be inherited from that of the prior carbon in the phase-separated region and is generally consistent with calculated literature values for gaseous diffusion rate-limited kinetic models.

Indentation measurements performed on the interlayer material revealed Young's moduli and microhardness values in the interlayer material that support the observed phase transformation sequence; however, measured hardness values in the present work contradict those reported by Bargeron et al. for the interlayer formed at temperatures up to 2060°C. This may indicate that the interlayer formed at much higher temperatures differs from that seen under the test conditions employed in the present work. Further study of the high-temperature oxidation behavior of HfC, especially at temperatures exceeding 1800°C, is recommended to resolve lingering discrepancies and to develop a comprehensive understanding of the high-temperature oxidation behavior of HfC.

ACKNOWLEDGMENTS

This material is based upon research supported by, or in part by, the U. S. Office of Naval Research under award number N00014-17-1-2931 (Dr. Eric Marineau, program officer, and Dr. Eric Wuchina, technical advisor). The authors gratefully acknowledge Dr. Eric Bohannon and the Missouri S&T Materials Research Center (MRC) and Advanced Materials Characterization Lab (AMCL) for use of facilities for X-ray diffraction and Raman spectroscopy analysis; University of Missouri Electron Microscopy Core Facility for assistance with SEM/FIB/TEM and partial funding through the Excellence in Electron Microscopy Award; and Dr. Matthew Maschmann, Dr. Cherian Joseph Mathai, and the University of Missouri Advanced Nanostructures Group for assistance with nanoindentation.

ORCID

David W. Lipke https://orcid.org/0000-0002-4557-6690

REFERENCES

1. Fleischer RL. High-temperature, high-strength materials – an overview. JOM. 1985;37(12):16–20.
2. Fahrenholtz WG, Wuchina EJ, Lee WE, Zhou Y. Ultra-high temperature ceramics materials for extreme environment applications. Hoboken, NJ: John Wiley & Sons; 2014.
3. Binner J, Porter M, Baker B, Zou J, Venkatachalam V, Diaz VR et al. Selection, processing, properties and applications of ultra-high temperature ceramic matrix composites, UHTCMCs – a review. Int Mater Rev. 2020;65(7):389–444.
4. Wang CR, Yang JM, Hoffman W. Thermal stability of refractory carbide/boride composites. Mater Chem Phys. 2002;74(3):272–81.
5. Okamoto H. The C-Hf (carbon-hafnium) system. Bull Alloy Phase Diagr. 1990;11:396–403.
6. Shin D, Arróyave R, Liu Z-K. Thermodynamic modeling of the Hf-Si-O system. Calphad. 2006;30(4):375–86.
7. Opeka MM, Talmy IG, Zaykoski JA. Oxidation-based materials selection for 2000°C + hypersonic aerosurfaces: theoretical considerations and historical experience. J Mater Sci. 2004;39:5887–904.
8. Wuchina, EJ, Opeka M. The oxidation behavior of HfC, HfN, and HfB_2. Electrochem Soc Proc. 2001;12:136–43.
9. Réjasse F, Rapaud O, Trolliard G, Masson O, Maître A. Experimental investigation and thermodynamic evaluation of the C–Hf–O ternary system. J Am Ceram Soc. 2017;100(8):3757–70.
10. Shimada S, Yunazar F, Otani S. Oxidation of hafnium carbide and titanium carbide single crystals with the formation of carbon at high temperatures and low oxygen pressures. J Am Ceram Soc. 2000;83(4):721–8.
11. Bargeron CB, Benson RC, Jette AN, Phillips TE. Oxidation of hafnium carbide in the temperature range 1400 to 2060°C. J Am Ceram Soc. 1993;76:1040–6.
12. Holcomb GR, St. Pierre GR. Application of a counter-current gaseous diffusion model to the oxidation of hafnium carbide at 1200 to 1530°C. Oxid Met. 1993;40(1–2):109–18.
13. ASTM International. Standard test methods for density of compacted or sintered powder metallurgy (PM) products using Archimedes' principle. In: ASTM B962-13. 2013. p. 1–7.
14. Gasparrini C, Podor R, Horlait D, Chater R, Lee WE. Zirconium carbide oxidation: Maltese cross formation and interface characterization. Oxid Met. 2017;88:509–19.
15. Shimada S. Oxidation and mechanism of single crystal carbides with formation of carbon. J Ceram Soc Jpn. 2001;109(3):S33–42.
16. Voitovich RF, Pugach EA. High-temperature oxidation of ZrC and HfC. Sov Powder Metall Met Ceram. 1973;12:916–21.
17. Metcalfe AG. Gas evolution during oxidation of refractory borides and carbides at 1500°C to 2700°C. ECS Trans. 2007;3(14):131–42.
18. Ferrari A, Robertson J. Interpretation of Raman spectra of disordered and amorphous carbon. Phys Rev B – Condens Matter Mater Phys. 2000;61(20):14095–107.
19. Ferrari AC. Raman spectroscopy of graphene and graphite: disorder, electron-phonon coupling, doping and nonadiabatic effects. Solid State Commun. 2007;143:47–57.
20. Mehltretter AH, Bradley MJ. Forensic analysis and discrimination of duct tapes. JASTEE. 2012;3(1):1–19.
21. Rodriguez-Navarro AB. Model of texture development in polycrystalline films growing on amorphous substrates with different topographies. Thin Solid Films. 2001;389:288–95.
22. Shimada S. TEM observation of the ZrC/ZrO_2 interface formed by oxidation of ZrC single crystals. J Mater Synth Process. 1998;6(3):191–5.

23. Sharma G, Ushakov SV, Navrotsky A. Size driven thermodynamic crossovers in phase stability in zirconia and hafnia. J Am Ceram Soc. 2018;101:31–5.
24. Luo X, Demkov AA. Structure, thermodynamics, and crystallization of amorphous hafnia. J Appl Phys. 2015;118:124105.
25. Parija A, Waetzig GR, Andrews JL, Banerjee S. Traversing energy landscapes away from equilibrium: strategies for accessing and utilizing metastable phase space. J Phys Chem C. 2018;122:25709–28.
26. Shakov SV, Navrotsky A, Yang Y, Stemmer S, Kukli K, Ritala M, et al. Crystallization in hafnia- and zirconia-based systems. Phys Status Solidi B. 2004;241(10):2268–78.
27. Wiatrowski A, Obstarczyk A, Mazur M, Kaczmarek D, Wojcieszak D. Characterization of HfO_2 optical coatings deposited by MF magnetron sputtering. Coatings. 2019;9:1–20
28. Sciti D, Guicciardi S, Nygren M. Densification and mechanical behavior of HfC and HfB_2 fabricated by spark plasma sintering. J Am Ceram Soc. 2008;91(5):1433–40.
29. Wang YL, Xiong X, Li GD, Liu HF, Chen Z, Sun Q, et al. Ablation behavior of HfC protective coatings for carbon/carbon composites in an oxyacetylene combustion flame. Corros Sci. 2012;65:549–55.

SUPPORTING INFORMATION

Additional supporting information can be found online in the Supporting Information section at the end of this article.

How to cite this article: Scott JA, He X, Lipke DW. The role of microstructure on high-temperature oxidation behavior of hafnium carbide. J Am Ceram Soc. 2022;1–11. https://doi.org/10.1111/jace.18941